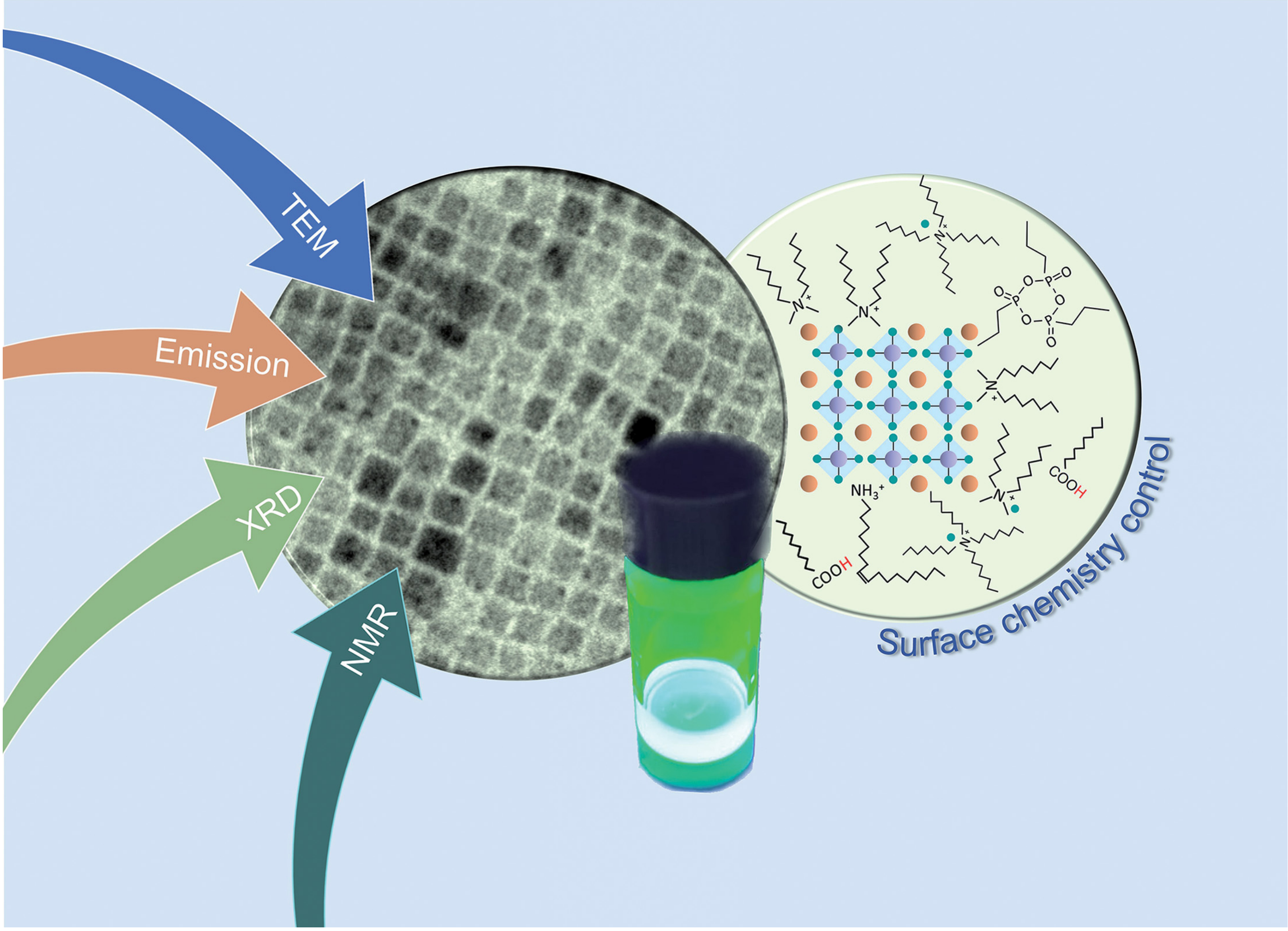

Showcasing research from Professor Fanizza's laboratory, Department of Chemistry, University of Studies of Bari, Italy

Molecular insights into the growth and time evolution of surface states of $CsPbBr_3$ nanoparticles synthesized using a scalable room temperature approach

A powerful investigation toolbox provided valuable insight on the complex molecular processes controlling size, reaction yield and emission properties of colloidal $CsPbBr_3$ nanoparticles, relevant for the development of up-scaled manufacturing of high quality materials for effective implementation in technological applications.

As featured in:

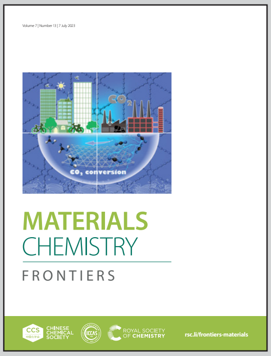

See Elisabetta Fanizza *et al.*, *Mater. Chem. Front.*, 2023, **7**, 2637.

CHINESE CHEMICAL SOCIETY
ROYAL SOCIETY OF CHEMISTRY
rsc.li/frontiers-materials

MATERIALS CHEMISTRY
FRONTIERS

CHINESE CHEMICAL SOCIETY

ROYAL SOCIETY OF CHEMISTRY

RESEARCH ARTICLE

View Article Online
View Journal | View Issue

Check for updates

Cite this: *Mater. Chem. Front.*, 2023, 7, 2637

Molecular insights into the growth and time evolution of surface states of $CsPbBr_3$ nanoparticles synthesized using a scalable room temperature approach†

Mariangela Giancaspro,[ab] Roberto Grisorio,[c] Gabriele Alò,[a] Nicola Margiotta,[a] Annamaria Panniello,[b] Gian Paolo Suranna,[cd] Nicoletta Depalo,[b] Marinella Striccoli,[be] M. Lucia Curri[ace] and Elisabetta Fanizza *[ace]

Received 9th March 2023,
Accepted 2nd May 2023

DOI: 10.1039/d3qm00243h

rsc.li/frontiers-materials

Room temperature ligand-assisted reprecipitation syntheses of $CsPbBr_3$ nanoparticles (NPs) under open air conditions and with non-polar solvents have recently emerged as viable strategies for large-scale production of highly emissive NPs. These procedures must meet some of the relevant requirements for industrial perspectives *i.e.* high-quality materials, low cost, and synthesis scalability. Here, starting from reported protocols, *ad hoc* mixtures in anhydrous toluene of precursors (Cs_2CO_3 and $PbBr_2$) and surfactants, such as oleylamine, alkylcarboxylic acid, didodecyldimethylammonium bromide, tetraoctylammonium bromide, octylphosphonic acid and phosphine oxide, are selected. The careful analysis of NP morphology, emission properties, reactive species in the mixtures and composition of the ligands bound at the NP surface or free in the final colloidal solution allows us to tackle still open issues, including the achievement of NP monodispersity, high NP production yield and to unveil the mechanisms behind changes in the emission properties over time. NP size dispersion is proved to depend not solely on ligand interaction with the NP surface, but also on the bromoplumbates species *in situ* generated in the reaction mixture upon caesium-precursor solution injection. Purification methods are carefully adjusted so as not to reduce the NP production yield, caused by aggregation phenomena induced by displacement of loosely bound ligands. Meanwhile, the residual species, left in the reaction mixture due to limited purification, are demonstrated to effectively contribute over time to the fate of the NP properties. Emission is exploited as effective macroscopic evidence of the NPs' molecular and structural modifications. In fact, the emission properties, which could be, in principle, predicted on the basis of the ligand density and binding energy, on long time scales are found to evolve over time due to the reaction of the residual molecules with the adsorbed ligands.

Introduction

Over the last few decades, colloidal all-inorganic lead halide perovskite (LHP) nanoparticles (NPs) have gained enormous interest, due to the plethora of their optical properties, including the high absorption coefficient in the visible range, efficient photoluminescence with narrow emission line widths and defect tolerant behaviour, advantageous for application in optoelectronic and photovoltaic devices.[1–7] The interest towards the technological application of this class of materials, driven by their unique characteristics, currently urges the quest for large-scale production methods, aiming at filling the gap between lab- and industrial scales. In this perspective the NPs also feature narrow size distribution[8] (standard deviation of the size below 15%) and long-term (optical and colloidal) stability,[9–12] highly desirable for device fabrication.

Since the pioneering work of Protesescu *et al.*,[13] reporting the synthesis of $CsPbBr_3$ NPs by means of a hot-injection (HI) method, many efforts have been put in the fundamental understanding of the dimensional control[14,15] and enhancement of the optical properties by purposely choosing the reactant

---

[a] *Chemistry Department, University of Bari, Via Orabona 4, 70126 Bari, Italy. E-mail: elisabetta.fanizza@uniba.it*
[b] *CNR-Institute for chemical physical processes (IPCF), Via Orabona 4, 70126 Bari, Italy*
[c] *Department of Civil, Environmental, Land, Construction and Chemistry (DICATECh), Polytechnic University of Bari, Via Orabona 4, 70125 Bari, Italy*
[d] *CNR-Institute of Nanotechnology (Nanotec), Via Monteroni, 73100 Lecce, Italy*
[e] *National Interuniversity Consortium of Materials Science and Technology, INSTM, Bari Research Unit, 70126, Bari, Italy*

† Electronic supplementary information (ESI) available. See DOI: **https://doi.org/10.1039/d3qm00243h**

composition and/or post-synthesis treatments. Although HI approaches can provide highly luminescent NPs, the fast defocusing of the size distribution within a few seconds from the injection, and shape purity, achievable only in a limited temperature range, make the ability to reach narrow size distribution a challenge to be tackled.[8] Furthermore, the use of a high-boiling solvent results in detrimental residual solvent traces in the final NP solution, even after purification. In addition, the energy cost, inherent to the HI method, and the air-free conditions, required for the synthesis, limit the industrial/large scale application of this synthetic approach.

Advantageously, the low crystallization energy of this class of materials enables their synthesis by room temperature solution procedures. Ligand-assisted reprecipitation (LARP) stands as the simplest method often put in place in open reactors that, by using basic chemistry apparatus and being inherently scalable, complies the needs for industrial production.[16] However, the conventional LARP approach, relying on the use of polar aprotic solvents to dissolve precursor salts and apolar non-solvents for NP crystallization, suffers from a low reaction yield, due to the poor solubility of the precursor salts (*i.e.* CsBr and $PbBr_2$).[16] Therefore new approaches have been developed, where the salt solubility has been increased by dissolving precursors in apolar aprotic solvents (*i.e.* toluene) in the presence of solvation agents (*i.e.* trioctylphosphine oxide – TOPO – and tetraoctylammonium bromide – TOAB –)[17–21] and ligands.[22] First[17,18] TOAB was used as the solvation and stabilizing agents, then the addition of less sterically hindered alkylammonium bromide was reported[19] to improve the NP stability. More recently, Brown *et al.*[21] employed phosphorous based solvation agents and ligands to afford size control and high emission properties.

NP surface engineering using a robust passivation layer, indeed, represents a feasible strategy to enhance the emission intensity and to limit the material intrinsic lability that causes optical and structural instability over time.[23]

Although $CsPbBr_3$ is a defect tolerant material, ligand composition has been demonstrated to affect the NP emission properties, making the interplay between the NP surface and the ligand shell, and between the ligands and the external environment, fundamental to obtaining robust and highly luminescent NPs for their implementation in technological applications. Improvements in electronic passivation[24,25] and colloidal stability[26] have been achieved by replacing primary amine ligands[24,27] with poorly sterically hindered quaternary alkylammonium salts,[18,28] that, instead, cannot exchange protons.[16,19,29–32] Phosphorous based compounds such as alkylphosphonic acid[21,33,34] have been also suggested as robust $CsPbBr_3$ ligands.[20]

Despite numerous efforts, how to concomitantly achieve NP monodispersity, high reaction yield and high emission, and which molecular processes are effectively involved, remain open issues.

Here we report inherently scalable polar-solvent free LARP approaches aiming at providing highly emissive and monodisperse NPs. To this purpose, *ad-hoc* composition of the reaction mixtures, based on precursors (Cs_2CO_3 and $PbBr_2$), ligands (*i.e.* oleylamine, Olam, didodecyldimethylammonium bromide, DDAB or phosphorous compounds in combination with an excess of alkyl carboxylic acid, oleic acid, OA, or nonanoic acid, NA), and solvation agents (TOAB or TOPO), jointly with a carefully designed purification process, are investigated. Three distinct series of NP samples with different ligands labelled NP_{Olam}, NP_{DDAB} and $NP_{OPA\ DDAB}$ are synthesized, and their resulting properties are rationalized. The molecular mechanisms underlying the high production yield, the NP size distribution and the time-evolution of the emission properties are clarified for each specific ligand/solvation agent pair, thanks to complementary morphological, spectroscopic, and compositional investigations. Indeed, interesting insights into the molecular control of the NP properties are gained, thus opening the venue to the implementation of novel cost-effective and scalable synthetic approaches for high quality $CsPbBr_3$ NPs.

Results and discussion

Ligand and solvation agents for the synthesis of monodispersed $CsPbBr_3$ NPs

Colloidal $CsPbBr_3$ NPs are synthesized by means of a polar solvent-free LARP approach.[16] According to this procedure, Cs_2CO_3 and $PbBr_2$ precursor salts are separately decomposed under mild reaction temperatures, in anhydrous toluene in the presence of solvation and coordinating agents. Unlike for HI methods,[13,35] here, inert conditions are not required, and precursor decomposition and NP syntheses are carried out in open-air. Then, the caesium-precursor is injected at room temperature into the lead/halide precursor solution, inducing the crystallization of the NPs (Fig. 1A), that can be subsequently recovered from the reaction mixture by further addition of an aprotic polar solvent (ethyl acetate, EtAc) and centrifugation steps. Toluene is finally used as the dispersant solvent. The use of toluene as the reaction solvent rather than high boiling solvents, generally used in HI, makes purification steps to get rid of leftovers in the final NP solution less critical.

In order to alleviate the limited solubility of the precursor salt in toluene,[18] solvation agents, like alkylcarboxylic acid (OA or NA) or alkylphosphine oxide (TOPO), acting as Lewis bases for Cs^+ and Pb^{2+}, respectively, or alkylammonium cation (TOAB) behaving as Lewis acids with halide ions, are added to the precursor solutions. Olam, along with alkylcarboxylic acid, or less sterically hindered alkylammonium bromide, such as DDAB, are here tested as ligands.[33,36–39]

Numerous sets of experiments using distinct ligand and solvation agent combinations are performed to systematically investigate the role of the reaction mixture composition in the kinetics of NP growth, surface passivation and NP stability, essential for providing a high NP production yield and NPs featuring good monodispersity, long term colloidal and optical stability. A summary of the most relevant preparative conditions is reported in Fig. 1B (see the Experimental section for NP synthesis and purification details).

All the performed syntheses use a large excess of $PbBr_2$ with respect to caesium ions ($PbBr_2/Cs^+ = 1/0.17$ molar ratio, see Fig. 1B)

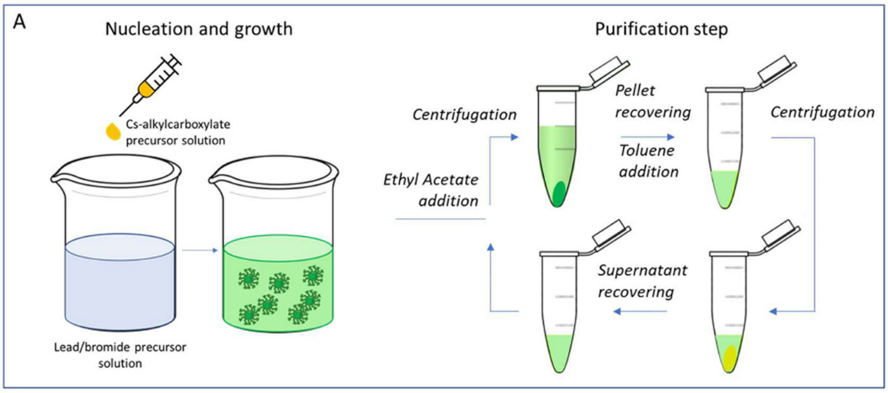

B Sample	$PbBr_2$: solvation agents/ligands molar ratio	*Cs^+/ligands molar ratio	*Additional Ligands molar ratio	Reaction time seconds	Purification
	$PbBr_2$: TOAB: Olam : OA	*Cs^+: OA	None	120	
NP_{Olam} 1	1 : 1.4: 1.5 : 2.6	0.17:2.5	---		Two-step
NP_{Olam} 2	1 : 1.4: 1.5 : 2.6	0.17:2.5	----		One-step
NP_{Olam} 3	1 : 0.7: 1.5 : 2.6	0.17:2.5			One-step
	$PbBr_2$: TOAB: DDAB : NA	*Cs^+: NA	None	300	
NP_{DDAB} 1	1 : 1.4: 0.60 : 2.6	0.17: 4.6			Two-step
NP_{DDAB} 2	1 : 1.4: 0.15 : 2.6	0.17: 4.6			Two-step
NP_{DDAB} 3	1 : 0.7: 0.30 : 2.6	0.17: 4.6			Two-step
	$PbBr_2$: TOPO: OPA	*Cs^+: NA	DDAB	300	
$NP_{OPA\ DDAB}$ 1	1 : 10: 0.7	0.17: 4.6	0.1		Two-step
$NP_{OPA\ DDAB}$ 2	1 : 10: 0.7	0.17: 4.6	0.1		One step

Fig. 1 (A) Schematic illustrations of the synthetic route and purification protocol employed for the room temperature synthesis of $CsPbBr_3$ nanoparticles. (B) Precursor solution composition and synthetic and purification conditions used for the synthesis of each NP sample. * The molar ratio values reported are calculated with respect to $PbBr_2$.

along with halide-rich conditions, provided by alkylammonium bromide, *i.e.* TOAB solvation agents or DDAB ligands, necessary to the formation of highly-coordinated bromoplumbate species, that, by caesium ion intercalation, "template" the perovskite structure. Meanwhile, under these conditions, the occurrence of bromide vacancies at the NP surface is expected to be limited, enhancing optical properties,[40] thanks to improved surface-trap passivation.

Furthermore, OA or NA, used in excess, react with Olam, when present in the reaction mixtures, shifting the acid–base equilibrium towards the formation of oleylammonium bromide, increasing the solubility of the bromide species. OA and NA activate the bromide, due to their reaction with alkylammonium bromide, yielding alkylammonium oleate (nonanoate) and hydrogen bromide. The latter, which is unstable in toluene, leads to additional release of bromide upon decomposition.[41] Fig. 2 reports the morphological (Fig. 2A–F) and spectroscopic (Fig. 2G and H) characterization of the NP_{Olam} (Fig. 2A–C and G) and NP_{DDAB} (Fig. 2D–F and H) sets of samples whose relevant geometrical features are reported in Fig. 3, together with the emission characteristics (emission peak wavelength and relative photoluminescence quantum yield, PL QY). The average lateral size, standard deviation of the size distribution (σ%) (Fig. S1 in the ESI†), absorption extinction coefficient values, as estimated by eqn (1)[42] (see the Experimental section), and NP concentration, evaluated by absorption measurement and Lambert–Beer law, allow the NP production yield to be estimated.

In the case of the NP_{Olam} sample set, regularly shaped nanocubes are obtained (Fig. 2A–C). The characterization of these samples, synthesized keeping the Olam content constant, clearly highlights that nanocube size and monodispersity depend on the purification procedure (see NP_{Olam} 1 *versus* NP_{Olam} 2 and NP $_{Olam}$ 3 Fig. 2 and 3) and TOAB solvation agents' content (see NP_{Olam} 2 *versus* NP_{Olam} 3 Fig. 2 and 3). It is worth pointing out that TOAB loosely coordinates the NP surface, due to steric hindrance of the long four alkyl chains, that place the ammonium positive charge too far from the NP surface to provide adequate stability.[31] Polydisperse (σ = 20%) nanocubes (Fig. 2A and 3A) with lateral size of 18 nm (NP_{Olam} 1), collected through two-step purification (see the Experimental section), turn into smaller nanocubes (10 nm, σ = 16%, NP_{Olam} 2, and 9 nm, σ = 9%, NP_{Olam} 3 Fig. 2B, C and 3A) when one-step purification is performed. Additionally, a reduction of the nanocube size distribution, with nearly the same average lateral size, is observed for the sample NP_{Olam} 3, synthesized by cutting the TOAB content in half. The large average size and lower NP production yield for NP_{Olam} 1 ([NP_{Olam} 3] > [NP_{Olam} 2] >> [NP_{Olam} 1], Fig. 3D) indicate poor NP stability against purification. Displacement of the ligands at the NP surface upon polar solvent addition[43] is expected to take place, which promotes the formation of aggregates, mostly removed by the centrifugation step, resulting in a decrease of the NP production yield. The UV-vis absorption and emission spectra of NP_{Olam} 1–3 (Fig. 2G) show the typical line profile of the $CsPbBr_3$ colloidal solution,

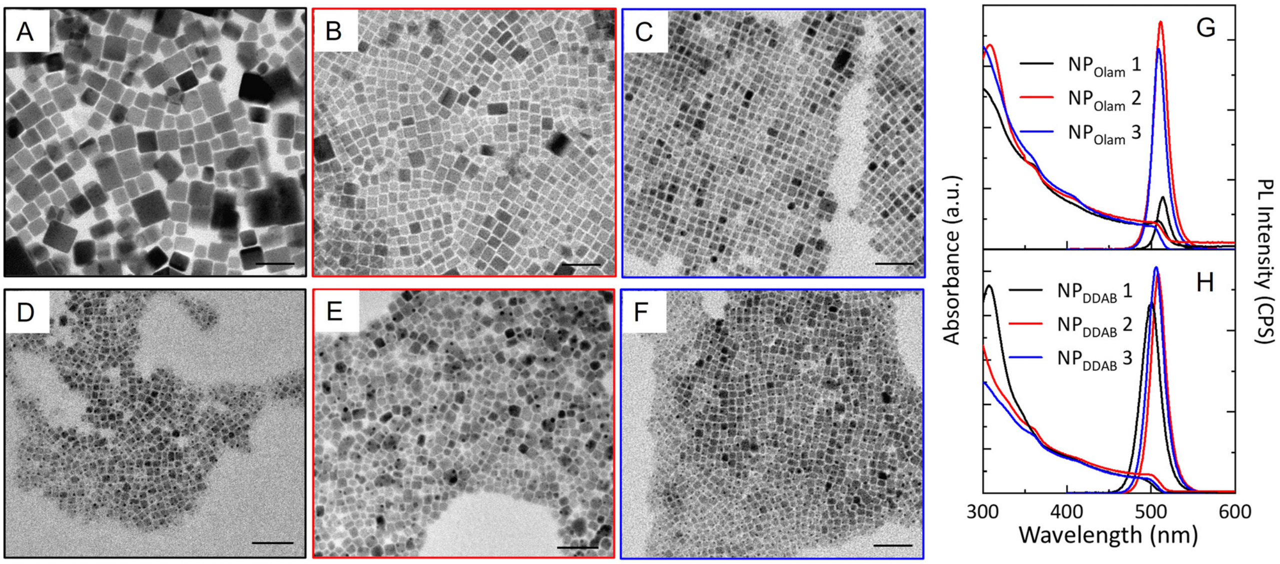

Fig. 2 (A–F) TEM micrographs (scale bar = 50 nm) and (G and H) UV-vis and PL spectra (λ_{ex} = 375 nm) of NP$_{Olam}$ 1–3 (A–C and G) and NP$_{DDAB}$ 1–3 (D–F and H); color code used for micrograph frames corresponding to those reported in panel G and H, respectively.

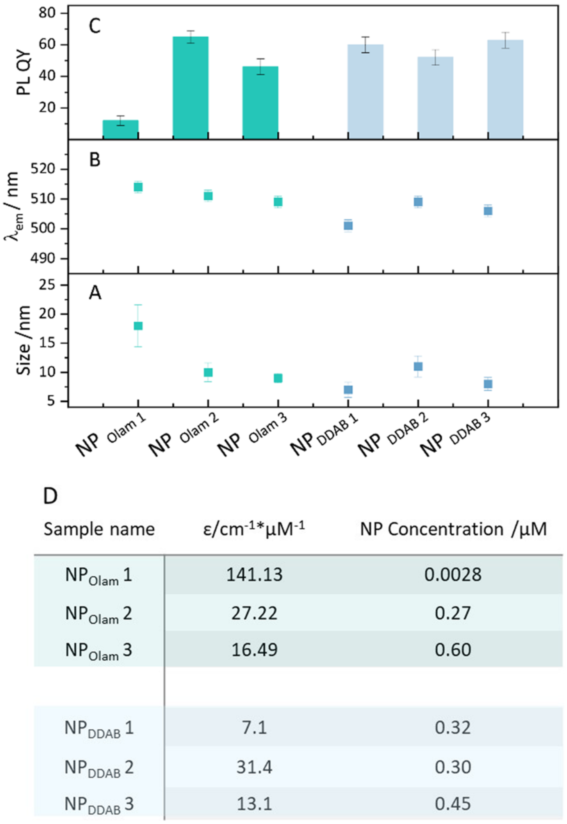

Sample name	ε/cm^{-1}*µM^{-1}	NP Concentration /µM
NP$_{Olam}$ 1	141.13	0.0028
NP$_{Olam}$ 2	27.22	0.27
NP$_{Olam}$ 3	16.49	0.60
NP$_{DDAB}$ 1	7.1	0.32
NP$_{DDAB}$ 2	31.4	0.30
NP$_{DDAB}$ 3	13.1	0.45

Fig. 3 (A) Scatter plots of nanoparticles' size (error bar size distribution) and (B) emission peak wavelength (λ_{ex} = 375 nm) and (C) PLQY value for all the selected samples. (D) Table of molar extinction coefficient ε at λ = 400 nm and concentration of colloidal nanoparticles.

and exciton transition and band edge recombination, whose position (Fig. 3B) agrees with that expected for weakly quantum-confined NPs of $CsPbBr_3$ (Bohr radius 3.5 nm). The trend in the relative PL QY NP$_{Olam}$ 1 $<<$ PL QY NP$_{Olam}$ 3 $<$ PL QY NP$_{Olam}$ 2 (Fig. 3C) can be discussed by taking into account the role of the size and surface passivation. It is worth noting that spatial confinement of the electron–hole pair, that increases the wavefunction overlap and the probability of radiative recombination, and trap-assisted recombination of excitons at the surface are competing processes affecting the emission properties and depend on size and surface passivation. Spatial confinement of electron–hole pairs mainly occurs by decreasing NP size, bringing a gradual increase in the NP PL QY as the NP size decreases.[44,45] Therefore, the NP$_{Olam}$ 1 sample, formed of large nanocubes, presents a low PL QY (12%), ascribable to the NP size far from quantum confinement and the possible presence of shallow traps arising from poor passivation (see Fig. S2 in the ESI†). Conversely, higher PL QY values are measured for NP$_{Olam}$ 2 (65%) and NP$_{Olam}$ 3 (46%) samples, which have, instead, sizes close to the Bohr radius (Fig. 3C). It is worth noting that the NP$_{Olam}$ 2 sample, synthesized in the presence of a large excess of TOAB, shows an absorption band centred at 312 nm, generally ascribed to residual highly coordinating $PbBr_6{}^{4-}$ species,[46] which is not completely removed after a one-step purification. This absorption feature is not detected in the spectrum of the NP$_{Olam}$ 3 sample, thus suggesting that at lower TOAB content one step purification is sufficient to remove the residual $PbBr_6{}^{4-}$ intermediates. A bromide-rich condition for the NP$_{Olam}$ 2 sample is therefore expected, which is beneficial for halide vacancies passivation, enhancing the radiative recombination path. Indeed, the average PL lifetimes of nearly 16.5 ns (±0.2) and 8.8 ns (±0.2), determined by the three-exponential fitting of the PL decay of NP$_{Olam}$ 2 and NP$_{Olam}$ 3, respectively (Fig. S2 in the ESI†), and the corresponding PL QY values suggest a higher density of states involved in radiative recombination for NP$_{Olam}$ 2. Conversely, faster recombination and PL QY $<$ 50% for NP$_{Olam}$ 3 suggest poorly passivated surface trap states.

For the NP_{DDAB} samples, prolonged reaction time (300 s) and lower molar content of DDAB, serving as the ligand, are found to be essential for NP formation and growth. Theoretical investigation and experimental results reported in the literature highlight that didodecyldimethyl ammonium ligands are less bulky than TOAB and can effectively bind the NP surface.[25] This NP ligand coating is more stable than that arising by primary oleylammonium interaction with the NP surface.[47] Moreover, recently, it has been pointed out that since alkyl ammonium bromides can promptly bind the NPs surface, the higher their concentration, the smaller the NPs.[48] Here, in agreement with these considerations, it is determined that a lower reaction time and/or high amount of DDAB do not result in any color change in the solution, indicating that NPs do not form or are too small (data not shown). A large excess of DDAB, promptly binding the NP surface, may hamper the addition of monomers at the NP surface, slowing down the kinetics of growth.[28,49] Conversely to what was reported by Song *et al.*,[19] DDAB needs to be added to the lead/halide precursor solution, to prevent irreversible aggregation right after caesium injection. NP_{DDAB} 1, synthesized using a $PbBr_2$: TOAB: DDAB molar ratio of 1 : 1.4 : 0.6, is characterized by an average lateral size of 7 nm (σ = 18%); NP_{DDAB} 2, prepared by reducing only the amount of DDAB ($PbBr_2$: TOAB : DDAB 1 : 1.4 : 0.15), presents larger NPs (11 nm, σ = 16%) (Fig. 2D, E and 3A). Sample NP_{DDAB} 3, where the amount of alkylammonium bromide salts, both TOAB and DDAB ($PbBr_2$: TOAB : DDAB 1 : 0.7 : 0.3 molar ratio, Fig. 2F) is reduced, shows NPs with an average lateral size of nearly 8 nm (σ = 16%). However, irrespectively from the ligands and solvation agents' content, all these samples feature NPs with a broad size distribution (Fig. 3). The PL QY, higher than 50%, the reproducible NPs concentration, above 0.3 μM (Fig. 3D), estimated for all the samples purified using the two-step procedure, prove that the NP_{DDAB} samples are robust against polar solvent (Fig. S3 in ESI†). DDA^+, featuring two C12 alkyl chains, provides a hydrophobic layer able to effectively protect the NP's surface from the polar solvent and a quaternary ammonium headgroup, which, not being susceptible to protonation, leads to a more stable and robust surface passivation, limiting NP aggregation and endowing them high emission.

To this point, it can be concluded that the use of DDAB ligands or large bromide content (NP_{Olam} 2) although able to effectively enhance NPs' PL QY, in fact, leads to a broad size distribution of the NPs. Conversely, the use of Olam, in an appropriate proportion with TOAB, as the solvation agent, brings about the formation of nanocubes with a narrow size distribution, although the labile ligands passivation is responsible for NP aggregation upon the addition of polar solvent and a decrease in their emission. To further understand how experimental conditions, and in particular, solvation agent and ligand composition, control the NP size distribution, the absorption spectra of reaction mixtures (RM) are recorded at different stages of the synthesis (Fig. 4A and B). The spectroscopic characterization can provide experimental evidence of the bromoplumbate species already in the RM or here released by *in situ* reaction, based on the association of the absorption profile to the specific bromoplumbate species: $PbBr_3^-$ and $PbBr_2$ show an absorption maximum at $\lambda_{max} = \sim 350$ nm, while $PbBr_5^{3-}$ has $\lambda_{max} = 275$ nm and $PbBr_6^{4-}$ $\lambda_{max} = 312$ nm in organic solvent.[50] The composition in bromoplumbates has been already reported to affect the dimensionality of the NPs,[51,52] with tridimensional perovskite structures arising from caesium ion intercalation between $PbBr_6^{4-}$ octahedra. To mimic the *in situ* reaction, avoiding nucleation/crystallization of the NPs, a toluene solution containing the sole OA or NA, at the same concentration used for the caesium precursors, without caesium salt, has been prepared and the appropriate volume added to the lead/bromide precursor solution either in the presence of Olam or DDAB ligands. Fig. 4A shows the absorption spectra of RM of the syntheses of NP_{Olam} 2 (Fig. 4A violet line) and NP_{Olam} 3 (Fig. 4A green line). While an absorption band at 312 nm, ascribed to $PbBr_6^{4-}$, appears in the RM_{Olam} 2 spectrum, RM_{Olam} 3 reveals an absorption profile that accounts for the presence of $PbBr_5^{3-}$. However, upon injection of the OA solution (Fig. 4A orange line), the spectrum suddenly changes, showing the absorption band characteristic of $PbBr_6^{4-}$. It could be assumed that by the addition

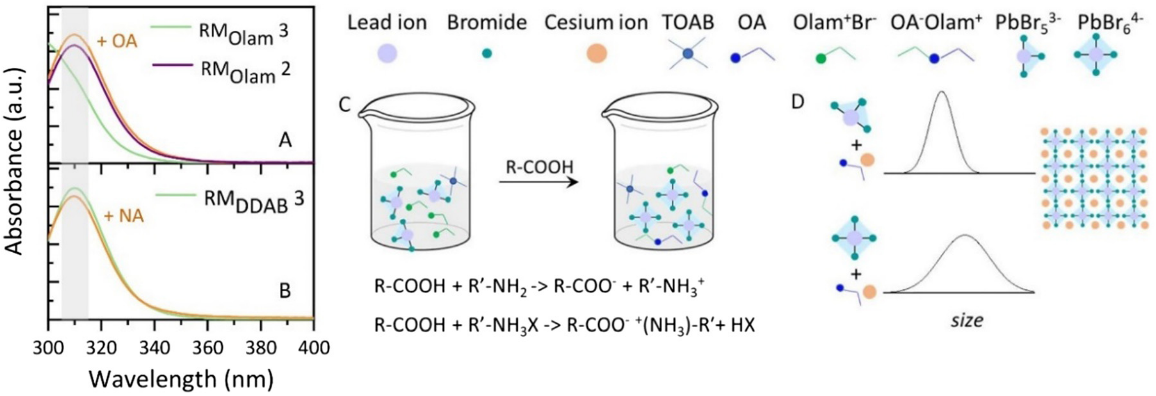

Fig. 4 UV absorption spectra of the reaction mixture (RM) used for the preparation of sample NP $_{Olam}$ 2 (violet line, panel A), NP $_{Olam}$ 3 before (green line, panel A) and after (orange line, panel A) the addition of oleic acid (OA) solution and NP $_{DDAB}$ 3 before (green line, panel B) and after (orange line, panel B) the addition of nonanoic acid (NA) solution. (C) Sketch of the reactions activated by alkyl carboxylic acid (R-COOH) addition in RM_{Olam} 3, triggering the formation of highly coordinated bromoplumbate species. (D) Schematic representation of the condition leading to monodispersed NPs.

of OA solution, more bromide ions are released from the OA reaction with oleylammonium bromide, so that the poorly bromide coordinated bromoplumbate species (*i.e.* $PbBr_5^{3-}$) turns into highly coordinated $PbBr_6^{4-}$, effective for NP formation (Fig. 4C). The replacement of OA with NA, a stronger alkyl carboxylic acid, brings the formation of $PbBr_6^{4-}$ already in the RM_{Olam} 3 (Fig. S4, ESI†) suggesting that the increase in acidity of the alkyl carboxylic acid shifts the equilibria towards the formation of oleylammonium bromides and HBr, resulting in NPs with a broad size distribution.

The results of this spectroscopic characterization combined with the outcome of the morphological characterization, indicate a correlation of the concomitant sudden formation of $PbBr_6^{4-}$ and release of caesium ions with the attainment of highly monodispersed NPs as for NP_{Olam} 3 (Fig. 4D). Conversely, injection of caesium ions in a solution where $PbBr_6^{4-}$ species are already formed, leads to NPs characterized by broader size distribution as the main products (as for NP_{Olam} 2, Fig. 4D). This is also confirmed by the NP_{DDAB} series (Fig. 4B): even for the RM featuring the lowest TOAB/DDAB content (RM_{DDAB} 3) the availability of bromide and of lead ions are sufficient to generate $PbBr_6^{4-}$, prior to the addition of NA or OA (Fig. S4, ESI†) solution, leading to NPs with a broad size distribution. Here the strength of the alkyl carboxylic acid, does not play any critical role in the regulation of the size distribution, since the bromoplumbates mainly depend on the alkyl ammonium bromide solvation and ligand content.

Time evolution of nanoparticle emission properties

NP_{Olam} 3 and NP_{DDAB} 3 samples, here named NP_{Olam} and NP_{DDAB} for the sake of clarity, are selected since they feature the same size and a higher yield of production among those of the same series. Optical investigation of these samples and of the $NP_{OPA\ DDAB}$ ones, which are synthesized following a polar-solvent free LARP approach reported in the literature with minor modification (see Fig. S5 in the ESI†), are performed. The steady-state emission spectra (Fig. 5A), PL QY (Fig. 5C), and TRPL decays (Fig. 5D) of the samples are discussed by considering NP concentration, surface passivation (Fig. 6 and 7), and time evolution of their properties (Fig. 8). The high production yield observed for NP_{Olam}, greater than that found for NP_{DDAB} and $NP_{OPA\ DDAB}$ (Fig. 5B), can be attributed to the kinetics of NP_{Olam} growth, that is not hampered by strong binding of the ligands.

The band gap calculated from the Tauc plot (Fig. S6 in the ESI†) is about 2.43 eV for NP_{DDAB} and $NP_{OPA\ DDAB}$ and slightly smaller (2.38 eV) for the larger NP_{Olam}, thus resulting within the typical range reported for $CsPbBr_3$ NPs and consistent with the size dependence of the band edge or surface passivation (Fig. 5E). The emission peak wavelength (Fig. 5A) slightly red shifts moving from $NP_{OPA\ DDAB}$, NP_{DDAB} and NP_{Olam} due to size, size distribution and different chemical environments determined by the surface capping layer. PL QY values (Fig. 5C, $NP_{OPA\ DDAB}$ 78% > NP_{DDAB} 63% > NP_{Olam} 46%) together with PL average lifetimes ⟨τ⟩ (Fig. 5D), which exhibit recombination dynamics faster for $NP_{OPA\ DDAB}$ (5.3 ns) and NP_{DDAB} (5.5 ns) than NP_{Olam} (8.8 ns) (Fig. 5E), indicate a higher density of radiative states for the $NP_{OPA\ DDAB}$ and NP_{DDAB} samples than NP_{Olam}. Since a size effect on the emission properties can be ruled out, due to the quite similar size of the compared samples, this kind of phenomenon can be thought to be related to the NPs passivation and stability of the ligands.

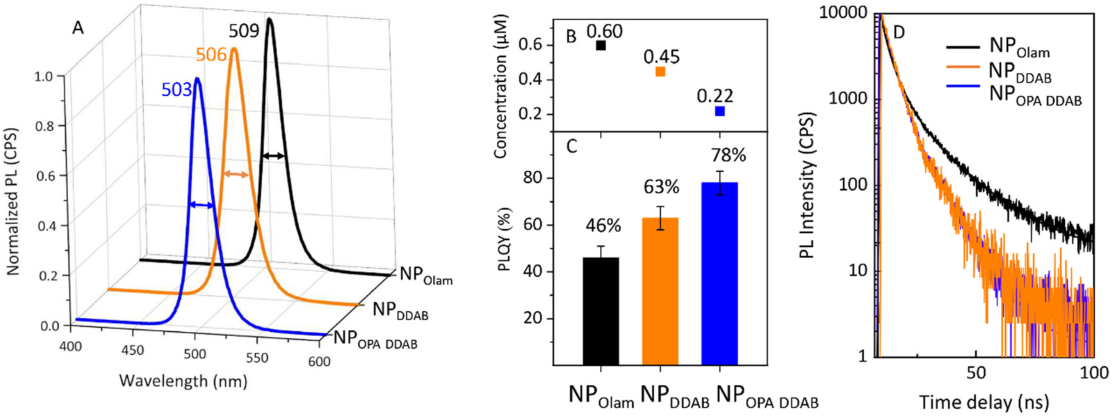

E

Sample	Size nm	σ (%)	Band gap eV	λ_{em} nm	FWHM (meV)	PLQY (%)	<τ> (ns)
NP_{Olam}	9	9	2.38	509	86	46±5	8.8±0.2
NP_{DDAB}	8	14	2.43	506	112	63±3	5.5±0.2
$NP_{OPA\ DDAB}$	8	13	2.42	503	93	78±4	5.3±0.2

Fig. 5 (A) Normalized PL emission spectra (λ_{ex} = 375 nm) with indication of emission peak wavelength (λ_{em}) and full width at half maximum (FWHM); (B) Scatter plot of the concentration, (C) bar plot of the PL quantum yield (PL QY) value and (D) time-resolved PL spectra of NP_{Olam} (black colour code), NP_{DDAB} (orange colour code), and $NP_{OPA\ DDAB}$ (blue colour code). (E) Table displaying relevant nanoparticles properties and optical features, such as size, size distribution, optical band gap, emission properties, including λ_{em} and FWHM, relative PL QY, average decay lifetime (τ) of the different samples.

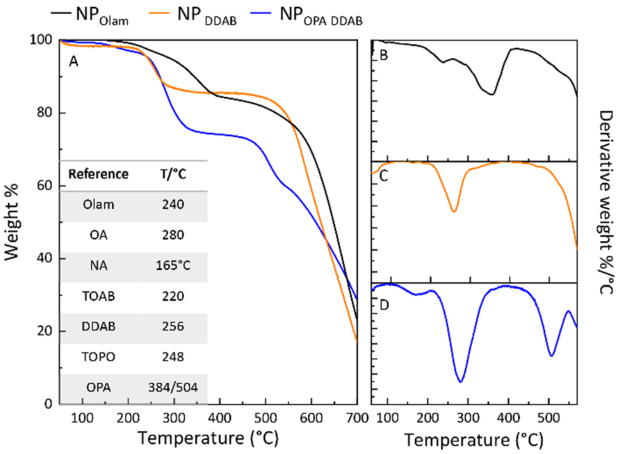

Fig. 6 (A) Thermogravimetric and (B–D) first derivative curves of NPOlam, NP$_{DDAB}$, and NP$_{OPA\ DDAB}$ and a table showing the evaporation temperature onset for pure ligands as a reference in panel A.[58,59]

To obtain insight into the NP and ligand shell composition and thus further elucidate NP ligand passivation, Energy Dispersive X-ray Analysis (EDX) was carried out for a semi-quantitative determination of the NP stoichiometry, while a complementary thermogravimetric and NMR characterization investigate the organic molecules composition, either bound or free. Cs : Pb : Br atomic ratio of 0.7 : 1 : 5 for NP$_{Olam}$, 1.4 : 1 : 6 for NP$_{DDAB}$ and 1.5 : 1 : 7 for NP$_{OPA\ DDAB}$ are calculated from EDX analysis. The resulting Br/Pb ratio > 3 appears consistent with bromide-rich synthetic conditions (Fig. S7 in the ESI†). Although a formal excess of PbBr$_2$ over caesium is always used in the synthesis, NP$_{DDAB}$ and NP$_{OPA\ DDAB}$ show a Cs/Pb ratio slightly higher than 1, while caesium deficient stoichiometry is calculated for NP$_{Olam}$. Therefore, CsBr-terminated CsPbBr$_3$ NPs[53] can be assumed for NP$_{DDAB}$ and NP$_{OPA\ DDAB}$, with caesium partially replaced by oleyl ammonium ions for NP$_{Olam}$.[54,55] Indeed, CsBr termination has already been demonstrated for cuboidal CsPbBr$_3$ nanocrystals, as the more thermodynamically favoured surface for NPs in the size range between 7–11 nm.[53] In fact, within this size regime, PbBr$_2$ termination is unlikely to occur as it would require much denser ligand packing, that would encounter significant steric hindrance, with the consequent disruption of the Pb^{2+} octahedral coordination.[53]

Thermogravimetric (TG) analysis has been performed under nitrogen flow on each NP sample collected as pellets after purification and drying at 50 °C, by applying a heating ramp

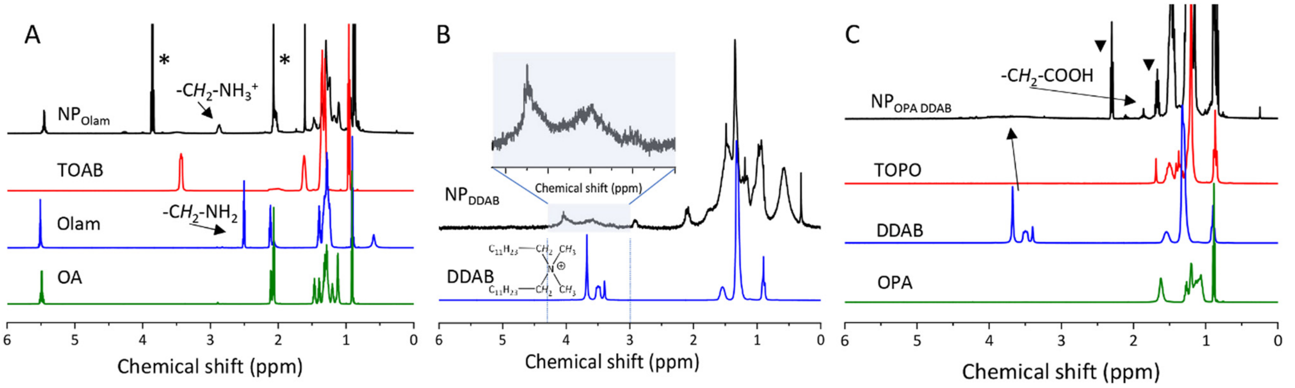

Fig. 7 1H-NMR spectra of the nanoparticles (black line) along with those of the solvation agents and ligands used during the synthesis as a reference. * indicates the peaks belonging to residual ethyl acetate (used for the purification stage). ▼ indicates the signals tentatively attributable to polyphosphonic anhydrides.

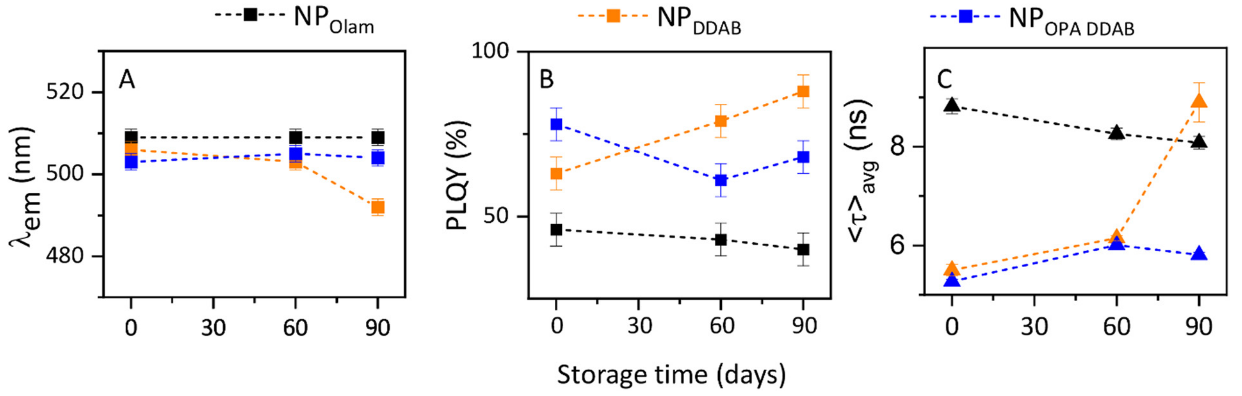

Fig. 8 Time evolution of (A) emission peak wavelength, (B) PL QY, and (C) average PL lifetime ($\langle\tau\rangle_{avg}$) for NP$_{Olam}$ (black line), NP$_{DDAB}$ (orange line) and NP$_{OPA\ DDAB}$ (blue line).

from 50 °C to 700 °C. TG and first derivative (DTG) curves are reported in Fig. 6. Above 550 °C, the weight loss could be reasonably ascribed to the $CsPbBr_3$ decomposition,[56,57] while the thermal events in the 50 °C and 550 °C temperature range arise from degradation of the tightly or weakly bound organic molecules of the NP shell. TG analysis can provide qualitative and quantitative information on the composition of the NP ligands and surface coverage by comparing the TG profile with those of pure ligands and solvation agents[58,59] used as the reference (Fig. S8 in the ESI† and the table in Fig. 6A). The evaporation of ligands chemically bound to the NP surface results in weight losses at high temperature and with a typically broadened TG profile.[58,60] A total weight loss of 35 wt% has been calculated for $NP_{OPA\ DDAB}$, while NP_{Olam} and NP_{DDAB} show nearly 15 wt% and 12 wt%, respectively. Since both $NP_{OPA\ DDAB}$ and NP_{Olam} underwent to the same one-step purification, the high weight loss for $NP_{OPA\ DDAB}$ can be attributed to residual molecules more resistant to removal by purification solvent. NP_{Olam} weight loss occurred in two temperature ranges: firstly between 175–263 °C, marked by a peak in the DTG curve centred at 236 °C (Fig. 6B), and a second one between 265–400 °C, with a major evaporation peak at 356 °C (Fig. 5B). Even though the TG profile does not allow discrimination between OA and Olam, the first weight loss could be associated with the elimination of free or physically adsorbed ligands, while the second one, covering a higher temperature range, to weight loss ascribed to evaporation of ligands bound to the surface of the NPs.[58]

The presence of residual free TOAB could not be ruled out in the NP_{Olam} sample nor in the NP_{DDAB} sample. This latter sample shows a single weight loss (nearly 12%) in the range from 225 °C and 280 °C, marked by a peak at 260 °C, associated to the loss of the DDAB bound to the NP surface. Weight losses over the ranges of 150–200 °C (4%), 228–330 °C (20%) and the steep one between 475–530 °C (11%) are shown for $NP_{OPA\ DDAB}$, ascribed to the evaporation of NA, DDAB and TOPO, OPA,[61] respectively (Fig. S8 in the ESI†).

A comparison of the ^{1}H-NMR spectra of the NPs in C_6D_6 with those of the ligands and solvation agents provides relevant insights in NP surface passivation. Signal broadening is due to ligands interacting with the NPs' surface, which causes a slower mobility in solution compared to the corresponding free ligands.[62,63] The ^{1}H NMR spectrum of the NP_{Olam} sample clearly shows the broad resonances of the methylene protons α-CH_2- of Olam in the 2.8–2.9 ppm range, with the resonance being broadened and shifted downfield compared to free oleyl amine as expected from bound oleylammonium (Fig. 6A). The ^{1}H NMR spectrum indicates that Olam is partially protonated, while OA, whose characteristic resonances preserve the fine structure at exactly the same chemical shift as the free molecule, is not bound to the NP surface and it is still protonated. The ^{1}H NMR spectra of NP_{DDAB} (Fig. 6B) and $NP_{OPA\ DDAB}$ (Fig. 6C) show a broad signal in the 3.2 to 4.1 ppm range, belonging to the surface-bound DDA^+ molecule. The chemical shifts of these broad peaks at a lower field compared to those of free DDAB molecules[32] are due to the different solvation at the surface of the NPs. Furthermore, the NMR spectrum of the $NP_{OPA\ DDAB}$ sample features multiple peaks in the range of 1.8–2.4 ppm tentatively attributed to polyphosphonic anhydrides that may have formed by condensation of phosphonic acids during the synthesis. It can be noted that the NMR spectrum of $NP_{OPA\ DDAB}$ does not show any signals ascribed to TOPO. This result suggests that it is largely removed by purification, though traces of TOPO cannot be ruled out. Residual NA, not adsorbed to the NP surface, is also detected, confirming the TGA characterization.

Following the nomenclature proposed by Bodnarchuk *et al.*,[24] the NPs can be conveniently written as $[CsPbBr_3]$-$(PbBr_2)_n\{AX\}_n$ structure where $[CsPbBr_3]$ is the inner core terminated by a $(PbBr_2)$ inner shell and a $\{AX\}$ outer shell. The outer $\{AX\}$ shell is composed of two types of A cations, Cs^+ and didodecyl dimethylammonium (DDA^+), with a slight excess of caesium ions for $NP_{OPA\ DDAB}$ and NP_{DDAB} and Cs^+ and oleyl ammonium, with a slight excess of oleylammonium for NP_{Olam}, and X type anions mainly Br^-. The lower PL QY for NP_{Olam} can be attributed to labile binding of oleylammonium.[36] On the other hand, DDAB,[24,64] passivating the surface of $NP_{OPA\ DDAB}$ and NP_{DDAB}, as Z-type ligands,[65] which could not lose or acquire protons, is capable of leading to a marked improvement of the NP stability, resulting in highly emissive NPs.

The time evolution of the PL QY and the PL recombination dynamics (Fig. 8 and Fig. S9–S11, ESI†) are monitored over time to evaluate the possible role of the specific surface chemistry on the modification of the emission properties. In principle, the ligands' dynamic exchanges and reactions with the environment can be assumed to be responsible for this evolution. The emission properties, being strongly correlated to the surface passivation, may provide prompt optical evidence of the mechanisms at the molecular/interface level that may affect the stability of NPs, or, alternatively, display how to limit them. Emission peak wavelength (Fig. 8A) remains unchanged for NP_{Olam} and $NP_{OPA\ DDAB}$, while a blue shift is measured for NP_{DDAB}, suggesting modification of the average size and/or size distribution. Statistical analysis of TEM micrographs (Fig. S12, ESI†) of this sample after 90 days of storage in air, indeed, reveals that NPs preserved the average lateral size (8 nm), assuming a more regular cuboidal structure than pristine ones, with a narrower size distribution (from $\sigma\% = 14\%$ to $\sigma\% = 10\%$).

In general, the emission properties of NP_{Olam} remain surprisingly unchanged after being stored in air for 90 days, unlike the generally reported deterioration of optical properties due to displacement of oleyl ammonium bromide caused by deprotonation. An explanation of this behaviour can be seen in the presence of residual free oleic acid molecules that sustain a large availability of oleylammonium bromide and limit its possible detachment from the NP surface upon air/humidity exposure (Scheme 1A). A marked increase in the PL QY (from 63% up to 88%, Fig. 8B) and of the PL lifetime (Fig. 8C) is observed for NP_{DDAB}, characterized by bound DDAB and free TOAB/DDAB molecules, which suggests better surface passivation. Imran *et al.*[31] reported a PL QY increase and a concomitant shrinking of the NP size upon addition of DDAB,

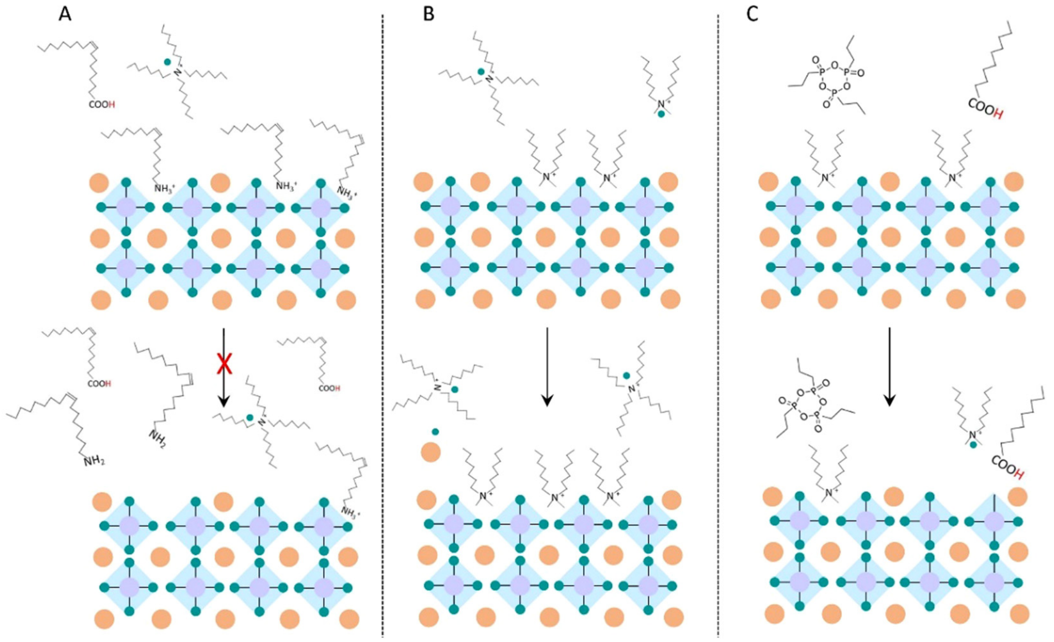

Scheme 1 Schematic representation of the dynamic time evolution of the NP ligand composition and stabilization.

explaining these findings with the exchange reaction of DDAB with NP outer shell components. A similar explanation can be here proposed for the investigated NP $_{\text{DDAB}}$. Over time, residual free DDAB can replace surface Cs–X, leading to a higher density of DDAB molecules binding the NP surface (Scheme 1B). This turns into an enhanced passivation with an organic shell resistant to ambient conditions, and an increase of the PL QY, while leading to a narrowing of the size distribution (Fig. S12, ESI†). On the other hand, the PLQY of the $NP_{\text{OPA DDAB}}$, though remaining high, decreases from 78% to 68% after 3 months (Fig. 8B). The in-depth investigation of carrier dynamics (Fig. 8C) reveals a decrease of the PL QY, an almost preserved average PL lifetime that suggests dominance of non-radiative processes over radiative ones over time, due to modification of the surface passivation and formation of surface trap-states. Simulations and empirical evidence reported by Zaccaria *et al.*[32] demonstrated that treatments with exogenous alkyl phosphonic and carboxylic acid molecules induce the stripping of DDA^+ from DDAB-passivated NPs, with a quenching of the luminescence. Similarly, it can be assumed that free protic NA (Scheme 1C), shown in the $NP_{\text{OPA DDAB}}$ by the TGA and NMR characterization, can displace the DDA^+ reducing ligand density and thus lead to trap state formation. Indeed, adsorption of NA as neutral L-ligands to Cs or Pb sites is not expected to occur, being an endergonic process. On the other hand, NA interaction as L^- replacing bromide as HBr cannot be expected either, as not favoured due to the higher pKa (4.9) of NA than HBr.[32]

Conclusions

Here, room temperature LARP approaches in non-polar solvents in air have been developed, defining for each pair of ligand/solvation agents the reaction mixtures most suited to obtain high NP production yields and NPs featuring enhanced emission.

The concomitant release of highly coordinated bromoplumbates species and caesium ions has been proved to lead to monodispersed samples; fast growth, not hampered by ligands strongly bound or ligands tolerant to purification treatments, have been demonstrated to favour high production yields. Residual species in the NP colloidal solution have been found to affect, over long time scales, the ligand shell stability, by taking part in reactions that can increase NP surface passivation or promote ligand displacements, affecting time-evolution of the emission properties.

Overall, this study has provided a deep insight into the complex molecular processes involved in the control of size, reaction yield and emission properties of colloidal $CsPbBr_3$ NPs, in view of the development of up-scale procedures offering high quality materials for effective implementation in relevant technological applications.

Experimental section

Materials

$PbBr_2$ (98%), Cs_2CO_3 (Alfa Aesar, 99.9%), nonanoic acid (NA, Sigma Aldrich, technical grade, 96%), oleic acid (OA, Sigma Aldrich, technical grade, 90%), oleyl amine (Olam, Sigma Aldrich, technical grade, 70%), didodecyl dimethylammonium bromide (DDAB, Sigma Aldrich, technical grade, 98%), octylphosphonic acid (OPA, 98%), trioctylphosphine oxide (TOPO, Sigma Aldrich, technical grade, 90%), anhydrous toluene (Sigma Aldrich, 99.8%), and ethyl acetate (EtAc, Sigma Aldrich, 99.8%).

Caesium precursor solution

Cs_2CO_3 (32.6 mg, 0.1 mmol) was dissolved in 1 mL of OA (3 mmol) or NA (5.6 mmol). The solution was heated at 80 °C in open air and stirred for 1 hour prior to its use. The Cs-oleate (0.2 M) and Cs-nonanoate (0.2 M) precursor solution was used for the synthesis of $CsPbBr_3$ NPs.

Synthesis and purification of $CsPbBr_3$ NP_{Olam}

A lead/bromide precursor solution was prepared by adding 165.2 mg (0.45 mmol) of $PbBr_2$, 330 mg (0.6 mmol) of TOAB and 360 μL (1.15 mmol) of OA to 3 ml of toluene resulting in $[PbBr_2]$ = 0.13 M, [TOAB] = 0.18 M, [OA] = 0.34 M. A second precursor solution was prepared by adding the same amount of $PbBr_2$ and OA, cutting in half the TOAB final concentration, 0.09 M. The precursor solution was heated at 70 °C for 15 min. For the synthesis of $CsPbBr_3$ NPs, 34 μL of a solution of Olam in toluene (0.3 M, 0.01 mmol) were added to 0.5 mL of each $PbBr_2$ precursor solution, followed by the injection of 55 μL of the Cs-oleate solution (11 μmol) under vigorous stirring at room temperature. Syntheses were also carried out from lead/bromide precursor solution prepared with NA, instead of OA, injecting Cs-nonanoate (Fig. S2, ESI†). After a further 120 s, EtAc was added as a non-solvent to precipitate the NPs.

Two purification procedures were tested to remove unreacted by-products and excesses of ligands and collect the NPs, namely a two-step and a single-step procedure.

For the two-step procedure, in the first stage, EtAc was added to the reaction mixture at a 3 : 1 v/v ratio and then the colloidal dispersion was centrifuged at 10 000 rpm for 10 minutes; the supernatant was discarded, and the precipitate was redispersed in 100 μL of toluene, followed by a second step of centrifugation at 5000 rpm. At this stage the supernatant was recovered for the second purification step. Finally, the pellet was redispersed in 1 mL of toluene.

For the one-step purification, a reaction mixture: EtAc 1 : 6 v/v ratio was used, and the NPs were collected by following the cycles of centrifugation/redispersion in toluene as previously described. These samples were labelled NP_{Olam}.

Synthesis and purification of $CsPbBr_3$ NP_{DDAB}

The lead/bromide precursor solution was prepared by adding 165.2 mg (0.45 mmol) of $PbBr_2$, 200 μL NA (1.15 mmol) and 330 mg (0.6 mmol) of TOAB to 3 mL of toluene, resulting in $[PbBr_2]$ = 0.14 M, [TOAB] = 0.19 M, [NA] = 0.36 M (or OA, at the same concentration). A second precursor solution was prepared by cutting in half the TOAB (0.09 M). The precursor solution was heated at 70 °C for 15 min. For the synthesis of the NPs, 15 mg (32.4 μmol) or 5 mg (10.8 μmol) or 10 mg (21.6 μmol) of DDAB were added to 0.5 ml of the lead/bromide precursor solution. The mixture was stirred at room temperature until DDAB completely dissolved. Then, 55 μL of the Cs-nonanoate solution (11 μmol) was quickly injected under vigorous stirring and the solution was stirred for 300 s. A shorter reaction time of 120 s was also tested. The two-step purification procedure was used to recover the NPs, remove the unreacted precursors and ligands, finally dispersing the NPs in 1 mL of toluene. These samples were labelled NP_{DDAB}.

Synthesis and purification of $CsPbBr_3$ $NP_{OPA\ DDAB}$

The synthesis was carried out according to the procedure reported by Brown *et al.*[21] with minor modifications. $PbBr_2$ 165.2 mg (0.45 mmol) was dissolved in toluene (3 mL) in the presence of TOPO (1.7 g, 4.5 mmol) and the flask was heated at 70 °C for 15 min prior to the addition of OPA (58 mg, 0.3 mmol). The precursor solution results in $[PbBr_2]$ = 0.15 M, [TOPO] = 0.15 M, [OPA] = 0.1 M. Cs-nonanoate solution (55 μL, 11 μmol) was injected in 0.5 mL of the lead/bromide precursor solution. After 30 s, 156 μL of a DDAB solution in toluene (0.05 M, 0.008 mmol) was added and after a further 300 s, the NP were recovered by addition of EtAc. Two-step and one-step purification procedures were performed. In particular, the one-step procedure was investigated by tuning the EtAc to the reaction mixture v/v ratio at 3 : 1, 1.5 : 1, and 1 : 1. The collected NPs were diluted in 1 mL of toluene. These samples were labelled $NP_{OPA\ DDAB}$.

Transmission electron microscopy (TEM)

TEM micrographs were acquired with a JEOL JEM1011 electronic microscope operating at 100 kV, equipped with a high-resolution CCD camera. Carbon-coated copper grids were dipped in the NPs colloidal solution diluted 1 : 20 with toluene letting the solvent evaporate.

UV-vis spectroscopy

UV-vis-NIR absorption spectra of all $CsPbBr_3$ NP samples were measured in 1 cm path length quartz cuvettes using a Cary Varian 5000 spectrophotometer supplied with a double detector. The absorption coefficient ε was calculated as reported by J. Maes, *et al.*,[42] according to the following equation:

$$\varepsilon = \frac{N_A \mu_i}{\ln 10} d^3 \qquad (1)$$

where μ_i is the intrinsic absorption coefficient and d is the average diameter, as calculated from TEM analysis.

Steady state PL and time-resolved photoluminescence measurements

Steady-state photoluminescence (PL) spectra and time resolved photoluminescence (TRPL) measurements were recorded for $CsPbBr_3$ colloidal solution with an optical absorption below 0.15. A HORIBA Jobin-Yvon Fluorolog 3 spectrofluorometer, equipped with double grating excitation and emission monochromators, was used to record the PL spectra, using an excitation wavelength at 375 nm, and TRPL measurements. The latter were carried out by using the Time-Correlated Single Photon Counting (TCSPC) technique using a picosecond laser diode (NanoLED 375L, excitation at 375 nm), with a pulse length of 80 ps and 1 MHz repetition rate. The PL signals were dispersed by a double grating monochromator and detected with a picosecond photon counter (TBX Photon Detection

Module, HORIBA Jobin-Yvon). The time resolution of the experimental set up was ∼200 ps.

The relative PL quantum yield of the $CsPbBr_3$ samples was estimated using Coumarin 153 in ethanol as the standard reference, including the correction for solvent refractive indices at 375 nm excitation wavelength, within the ratio calculation. The PLQY of Coumarin 153 in ethanol is taken as 38%.[66]

Nuclear magnetic resonance (NMR)

^{1}H-NMR spectra were recorded on an Agilent 500/54 Premium shielded spectrometer. ^{1}H chemical shifts were referenced using the internal residual peak of the solvent (C_6D_6, δ 7.16 ppm).

Thermogravimetric analysis (TGA)

TGA was carried out using a Pyris 1-PerkinElmer instrument under a nitrogen flow of 40 mL min^{-1} at the heating rate of 20 °C min^{-1} in a temperature range from 50 °C to 700 °C. Thermograms were collected using the powder of dried NP samples.

EDX analysis

Elemental analyses of the powders were performed by Energy Dispersive X-ray Analysis (EDX) on a Field Emission Sigma Zeiss SEM microscope (ZEISS, ΣIGMA) equipped with a LaB_6 source thermal field emitter and a Gemini objective lens. The samples for EDX characterization were prepared by drop casting the NP colloidal dispersion solutions onto an extensively washed silica substrate. The measurements were performed at a working distance of 7 mm and an electron generation voltage of 15 keV.

Author contributions

Ms M. Giancaspro: conceptualisation, investigation, visualisation, and writing – original draft; Prof. R. Grisorio: investigation, writing – original draft and writing – review and editing; Mr G. Alò: investigation and visualization; Prof. N. Margiotta: investigation, visualisation, and writing – review and editing; Dr A. Panniello: supervision, visualization, and writing – review and editing; Prof. G. P. Suranna: visualization and writing – review and editing; Dr N. Depalo: visualization and writing – review and editing Dr M. Striccoli: visualization, funding acquisition and writing – review and editing; Prof. M. L. Curri: visualization, funding acquisition and writing – review and editing; Prof. E. Fanizza: conceptualisation, supervision, investigation, visualisation, writing – original draft, and writing – review and editing.

Conflicts of interest

There are no conflicts to declare.

Acknowledgements

The authors thank Dr R. Castaldo and Dr G. Gentile, from the CNR-Institute of Polymers, Composites and Biomaterials (CNR-IPCB) for their support and fruitful discussion in thermogravimetric analysis. The Italia PON R&I ECOTEC (2014–2020 ARS01_00951) and the Project titled ''Network 4 Energy Sustainable Transition – NEST'', project code PE0000021, Concession Decree No. 1561 of 11.10.2022 adopted by Ministero dell'Università e della Ricerca (MUR), CUP B53C22004060006, funded by the European Union– NextGenerationEU under the National Recovery and Resilience Plan (NRRP), Mission 4 Component 2 Investment 1.3 – Call for tender No. 1561 of 11.10.2022 of Ministero dell'Università e della Ricerca (MUR) are grateful acknowledged.

References

1 M. V. Kovalenko, L. Protesescu and M. I. Bodnarchuk, Properties and potential optoelectronic applications of lead halide perovskite nanocrystals, *Science*, 2017, **358**, 745–750.

2 H. Huang, M. I. Bodnarchuk, S. V. Kershaw, M. V. Kovalenko and A. L. Rogach, Lead Halide Perovskite Nanocrystals in the Research Spotlight: Stability and Defect Tolerance, *ACS Energy Lett.*, 2017, **2**, 2071–2083.

3 Q. A. Akkerman, G. Rainò, M. V. Kovalenko and L. Manna, Genesis, challenges and opportunities for colloidal lead halide perovskite nanocrystals, *Nat. Mater.*, 2018, **17**, 394–405.

4 J. Cui, Y. Liu, Y. Deng, C. Lin, Z. Fang, C. Xiang, P. Bai, K. Du, X. Zuo, K. Wen, S. Gong, H. He, Z. Ye, Y. Gao, H. Tian, B. Zhao, J. Wang and Y. Jin, Efficient light-emitting diodes based on oriented perovskite nanoplatelets, *Sci. Adv.*, 2021, **7**, eabg8458.

5 M. Liu, Q. Wan, H. Wang, F. Carulli, X. Sun, W. Zheng, L. Kong, Q. Zhang, C. Zhang, Q. Zhang, S. Brovelli and L. Li, Suppression of temperature quenching in perovskite nanocrystals for efficient and thermally stable light-emitting diodes, *Nat. Photonics*, 2021, **15**, 379–385.

6 J. Wang, Y. Xu, S. Zou, C. Pang, R. Cao, Z. Pan, C. Guo, S. Hu, J. Liu, Z. Xie and Z. Gong, Effective defect passivation of CsPbBr3 quantum dots using gallium cations toward the fabrication of bright perovskite LEDs, *J. Mater. Chem. C*, 2021, **9**, 11324–11330.

7 L. Cheng, J. Chi, M. Su and Y. Song, Interface engineering of perovskite nanocrystals: challenges and opportunities for biological imaging and detection, *J. Mater. Chem. C*, 2023, DOI: 10.1039/D2TC04967H.

8 G. Almeida, L. Goldoni, Q. Akkerman, Z. Dang, A. H. Khan, S. Marras, I. Moreels and L. Manna, Role of Acid–Base Equilibria in the Size, Shape, and Phase Control of Cesium Lead Bromide Nanocrystals, *ACS Nano*, 2018, **12**, 1704–1711.

9 R. Grisorio, F. Fasulo, A. B. Muñoz-García, M. Pavone, D. Conelli, E. Fanizza, M. Striccoli, I. Allegretta, R. Terzano, N. Margiotta, P. Vivo and G. P. Suranna, In Situ Formation of Zwitterionic Ligands: Changing the Passivation Paradigms of CsPbBr3 Nanocrystals, *Nano Lett.*, 2022, **22**, 4437–4444.

10 E. Fanizza, F. Cascella, D. Altamura, C. Giannini, A. Panniello, L. Triggiani, F. Panzarea, N. Depalo, R. Grisorio,

G. P. Suranna, A. Agostiano, M. L. Curri and M. Striccoli, Post-synthesis phase and shape evolution of CsPbBr3 colloidal nanocrystals: The role of ligands, *Nano Res.*, 2019, **12**, 1155–1166.

11 Y. Zhang, G. Li, C. She, S. Liu, F. Yue, C. Jing, Y. Cheng and J. Chu, Room temperature preparation of highly stable cesium lead halide perovskite nanocrystals by ligand modification for white light-emitting diodes, *Nano Res.*, 2021, **14**, 2770–2775.

12 M. Pols, T. Hilpert, I. A. W. Filot, A. C. T. van Duin, S. Calero and S. Tao, What Happens at Surfaces and Grain Boundaries of Halide Perovskites: Insights from Reactive Molecular Dynamics Simulations of CsPbI3, *ACS Appl. Mater. Interfaces*, 2022, **14**, 40841–40850.

13 L. Protesescu, S. Yakunin, M. I. Bodnarchuk, F. Krieg, R. Caputo, C. H. Hendon, R. X. Yang, A. Walsh and M. V. Kovalenko, Nanocrystals of Cesium Lead Halide Perovskites (CsPbX3, X = Cl, Br, and I): Novel Optoelectronic Materials Showing Bright Emission with Wide Color Gamut, *Nano Lett.*, 2015, **15**, 3692–3696.

14 X. Zheng, Y. Hou, H.-T. Sun, O. F. Mohammed, E. H. Sargent and O. M. Bakr, Reducing Defects in Halide Perovskite Nanocrystals for Light-Emitting Applications, *J. Phys. Chem. Lett.*, 2019, **10**, 2629–2640.

15 C. Otero-Martínez, D. García-Lojo, I. Pastoriza-Santos, J. Pérez-Juste and L. Polavarapu, Dimensionality Control of Inorganic and Hybrid Perovskite Nanocrystals by Reaction Temperature: From No-Confinement to 3D and 1D Quantum Confinement, *Angew. Chem., Int. Ed.*, 2021, **60**, 26677–26684.

16 A. A. M. Brown, B. Damodaran, L. Jiang, J. N. Tey, S. H. Pu, N. Mathews and S. G. Mhaisalkar, Lead Halide Perovskite Nanocrystals: Room Temperature Syntheses toward Commercial Viability, *Adv. Energy Mater.*, 2020, **10**, 2001349.

17 S. Wei, Y. Yang, X. Kang, L. Wang, L. Huang and D. Pan, Room-temperature and gram-scale synthesis of CsPbX3 (X = Cl, Br, I) perovskite nanocrystals with 50–85% photoluminescence quantum yields, *Chem. Commun.*, 2016, **52**, 7265–7268.

18 S. Wei, Y. Yang, X. Kang, L. Wang, L. Huang and D. Pan, Homogeneous Synthesis and Electroluminescence Device of Highly Luminescent CsPbBr3 Perovskite Nanocrystals, *Inorg. Chem.*, 2017, **56**, 2596–2601.

19 J. Song, J. Li, L. Xu, J. Li, F. Zhang, B. Han, Q. Shan and H. Zeng, Room-Temperature Triple-Ligand Surface Engineering Synergistically Boosts Ink Stability, Recombination Dynamics, and Charge Injection toward EQE-11.6% Perovskite QLEDs, *Adv. Mater.*, 2018, **30**, 1800764.

20 K. Dave, Z. Bao, S. Nakahara, K. Ohara, S. Masada, H. Tahara, Y. Kanemitsu and R.-S. Liu, Improvement in quantum yield by suppression of trions in room temperature synthesized CsPbBr3 perovskite quantum dots for backlight displays, *Nanoscale*, 2020, **12**, 3820–3826.

21 A. A. M. Brown, P. Vashishtha, T. J. N. Hooper, Y. F. Ng, G. V. Nutan, Y. Fang, D. Giovanni, J. N. Tey, L. Jiang, B. Damodaran, T. C. Sum, S. H. Pu, S. G. Mhaisalkar and N. Mathews, Precise Control of CsPbBr3 Perovskite Nanocrystal Growth at Room Temperature: Size Tunability and Synthetic Insights, *Chem. Mater.*, 2021, **33**, 2387–2397.

22 C. M. Guvenc, A. Kocabas and S. Balci, Polar solvent-free room temperature synthesis of CsPbX3 (X = Br, Cl) perovskite nanocubes, *J. Mater. Chem. C*, 2023, **11**, 3039–3049.

23 W. Yan, J. Shen, Y. Zhu, Y. Gong, J. Zhu, Z. Wen and C. Li, CsPbBr3 quantum dots photodetectors boosting carrier transport via molecular engineering strategy, *Nano Res.*, 2021, **14**, 4038–4045.

24 M. I. Bodnarchuk, S. C. Boehme, S. ten Brinck, C. Bernasconi, Y. Shynkarenko, F. Krieg, R. Widmer, B. Aeschlimann, D. Günther, M. V. Kovalenko and I. Infante, Rationalizing and Controlling the Surface Structure and Electronic Passivation of Cesium Lead Halide Nanocrystals, *ACS Energy Lett.*, 2019, **4**, 63–74.

25 J. H. Park, A.-y Lee, J. C. Yu, Y. S. Nam, Y. Choi, J. Park and M. H. Song, Surface Ligand Engineering for Efficient Perovskite Nanocrystal-Based Light-Emitting Diodes, *ACS Appl. Mater. Interfaces*, 2019, **11**, 8428–8435.

26 D. Quarta, M. Imran, A.-L. Capodilupo, U. Petralanda, B. van Beek, F. De Angelis, L. Manna, I. Infante, L. De Trizio and C. Giansante, Stable Ligand Coordination at the Surface of Colloidal CsPbBr3 Nanocrystals, *J. Phys. Chem. Lett.*, 2019, **10**, 3715–3726.

27 S. ten Brinck, F. Zaccaria and I. Infante, Defects in Lead Halide Perovskite Nanocrystals: Analogies and (Many) Differences with the Bulk, *ACS Energy Lett.*, 2019, **4**, 2739–2747.

28 W. Zheng, Z. Li, C. Zhang, B. Wang, Q. Zhang, Q. Wan, L. Kong and L. Li, Stabilizing perovskite nanocrystals by controlling protective surface ligands density, *Nano Res.*, 2019, **12**, 1461–1465.

29 M. Imran, P. Ijaz, D. Baranov, L. Goldoni, U. Petralanda, Q. Akkerman, A. L. Abdelhady, M. Prato, P. Bianchini, I. Infante and L. Manna, Shape-Pure, Nearly Monodispersed CsPbBr3 Nanocubes Prepared Using Secondary Aliphatic Amines, *Nano Lett.*, 2018, **18**, 7822–7831.

30 Y. Miao, Y. Chen, H. Chen, X. Wang and Y. Zhao, Using steric hindrance to manipulate and stabilize metal halide perovskites for optoelectronics, *Chem. Sci.*, 2021, **12**, 7231–7247.

31 M. Imran, P. Ijaz, L. Goldoni, D. Maggioni, U. Petralanda, M. Prato, G. Almeida, I. Infante and L. Manna, Simultaneous Cationic and Anionic Ligand Exchange For Colloidally Stable CsPbBr3 Nanocrystals, *ACS Energy Lett.*, 2019, **4**, 819–824.

32 F. Zaccaria, B. Zhang, L. Goldoni, M. Imran, J. Zito, B. van Beek, S. Lauciello, L. De Trizio, L. Manna and I. Infante, The Reactivity of CsPbBr3 Nanocrystals toward Acid/Base Ligands, *ACS Nano*, 2022, **16**, 1444–1455.

33 Y. Tan, Y. Zou, L. Wu, Q. Huang, D. Yang, M. Chen, M. Ban, C. Wu, T. Wu, S. Bai, T. Song, Q. Zhang and B. Sun, Highly Luminescent and Stable Perovskite Nanocrystals with Octylphosphonic Acid as a Ligand for Efficient Light-Emitting Diodes, *ACS Appl. Mater. Interfaces*, 2018, **10**, 3784–3792.

34 B. Zhang, L. Goldoni, C. Lambruschini, L. Moni, M. Imran, A. Pianetti, V. Pinchetti, S. Brovelli, L. De Trizio and

L. Manna, Stable and Size Tunable CsPbBr3 Nanocrystals Synthesized with Oleylphosphonic Acid, *Nano Lett.*, 2020, **20**, 8847–8853.

35 Q. A. Akkerman, V. D'Innocenzo, S. Accornero, A. Scarpellini, A. Petrozza, M. Prato and L. Manna, Tuning the Optical Properties of Cesium Lead Halide Perovskite Nanocrystals by Anion Exchange Reactions, *J. Am. Chem. Soc.*, 2015, **137**, 10276–10281.

36 B. Zhang, L. Goldoni, J. Zito, Z. Dang, G. Almeida, F. Zaccaria, J. de Wit, I. Infante, L. De Trizio and L. Manna, Alkyl Phosphonic Acids Deliver CsPbBr3 Nanocrystals with High Photoluminescence Quantum Yield and Truncated Octahedron Shape, *Chem. Mater.*, 2019, **31**, 9140–9147.

37 G. Almeida, O. J. Ashton, L. Goldoni, D. Maggioni, U. Petralanda, N. Mishra, Q. A. Akkerman, I. Infante, H. J. Snaith and L. Manna, The Phosphine Oxide Route toward Lead Halide Perovskite Nanocrystals, *J. Am. Chem. Soc.*, 2018, **140**, 14878–14886.

38 Y. Shynkarenko, M. I. Bodnarchuk, C. Bernasconi, Y. Berezovska, V. Verteletskyi, S. T. Ochsenbein and M. V. Kovalenko, Direct Synthesis of Quaternary Alkylammonium-Capped Perovskite Nanocrystals for Efficient Blue and Green Light-Emitting Diodes, *ACS Energy Lett.*, 2019, **4**, 2703–2711.

39 S. Gutiérrez Álvarez, W. Lin, M. Abdellah, J. Meng, K. Žídek, T. Pullerits and K. Zheng, Charge Carrier Diffusion Dynamics in Multisized Quaternary Alkylammonium-Capped CsPbBr3 Perovskite Nanocrystal Solids, *ACS Appl. Mater. Interfaces*, 2021, **13**, 44742–44750.

40 Y. Wu, C. Wei, X. Li, Y. Li, S. Qiu, W. Shen, B. Cai, Z. Sun, D. Yang, Z. Deng and H. Zeng, In Situ Passivation of PbBr64− Octahedra toward Blue Luminescent CsPbBr3 Nanoplatelets with Near 100% Absolute Quantum Yield, *ACS Energy Lett.*, 2018, **3**, 2030–2037.

41 J.-R. Wen, F. A. Rodríguez Ortiz, A. Champ and M. T. Sheldon, Kinetic Control for Continuously Tunable Lattice Parameters, Size, and Composition during CsPbX3 (X = Cl, Br, I) Nanorod Synthesis, *ACS Nano*, 2022, **16**, 8318–8328.

42 J. Maes, L. Balcaen, E. Drijvers, Q. Zhao, J. De Roo, A. Vantomme, F. Vanhaecke, P. Geiregat and Z. Hens, Light Absorption Coefficient of CsPbBr3 Perovskite Nanocrystals, *J. Phys. Chem. Lett.*, 2018, **9**, 3093–3097.

43 Y. Kuang, C. Zhu, W. He, X. Wang, Y. He, X. Ran and L. Guo, Regulated Exciton Dynamics and Optical Properties of Single Perovskite CsPbBr3 Quantum Dots by Diluting Surface Ligands, *J. Mater. Chem. C*, 2020, **124**, 23905–23912.

44 Y. H. Kim, C. Wolf, Y. T. Kim, H. Cho, W. Kwon, S. Do, A. Sadhanala, C. G. Park, S. W. Rhee, S. H. Im, R. H. Friend and T. W. Lee, Highly Efficient Light-Emitting Diodes of Colloidal Metal-Halide Perovskite Nanocrystals beyond Quantum Size, *ACS Nano*, 2017, **11**, 6586–6593.

45 M. C. Brennan, J. E. Herr, T. S. Nguyen-Beck, J. Zinna, S. Draguta, S. Rouvimov, J. Parkhill and M. Kuno, Origin of the Size-Dependent Stokes Shift in CsPbBr3 Perovskite Nanocrystals, *J. Am. Chem. Soc.*, 2017, **139**, 12201–12208.

46 J. C. Dahl, X. Wang, X. Huang, E. M. Chan and A. P. Alivisatos, Elucidating the Weakly Reversible Cs–Pb–Br Perovskite Nanocrystal Reaction Network with High-Throughput Maps and Transformations, *J. Am. Chem. Soc.*, 2020, **142**, 11915–11926.

47 A. Stelmakh, M. Aebli, A. Baumketner and M. V. Kovalenko, On the Mechanism of Alkylammonium Ligands Binding to the Surface of CsPbBr3 Nanocrystals, *Chem. Mater.*, 2021, **33**, 5962–5973.

48 A. Dutta, S. K. Dutta, S. Das Adhikari and N. Pradhan, Tuning the Size of CsPbBr3 Nanocrystals: All at One Constant Temperature, *ACS Energy Lett.*, 2018, **3**, 329–334.

49 Y. Huang, W. Luan, M. Liu and L. Turyanska, DDAB-assisted synthesis of iodine-rich CsPbI3 perovskite nanocrystals with improved stability in multiple environments, *J. Mater. Chem. C*, 2020, **8**, 2381–2387.

50 R. Grisorio, D. Conelli, E. Fanizza, M. Striccoli, D. Altamura, C. Giannini, I. Allegretta, R. Terzano, M. Irimia-Vladu, N. Margiotta and G. P. Suranna, Size-tunable and stable cesium lead-bromide perovskite nanocubes with near-unity photoluminescence quantum yield, *Nanoscale Adv.*, 2021, **3**, 3918–3928.

51 R. Grisorio, E. Fanizza, I. Allegretta, D. Altamura, M. Striccoli, R. Terzano, C. Giannini, V. Vergaro, G. Ciccarella, N. Margiotta and G. P. Suranna, Insights into the role of the lead/surfactant ratio in the formation and passivation of cesium lead bromide perovskite nanocrystals, *Nanoscale*, 2020, **12**, 623–637.

52 R. Grisorio, D. Conelli, R. Giannelli, E. Fanizza, M. Striccoli, D. Altamura, C. Giannini, I. Allegretta, R. Terzano and G. P. Suranna, A new route for the shape differentiation of cesium lead bromide perovskite nanocrystals with near-unity photoluminescence quantum yield, *Nanoscale*, 2020, **12**, 17053–17063.

53 S. R. Smock, Y. Chen, A. J. Rossini and R. L. Brutchey, The Surface Chemistry and Structure of Colloidal Lead Halide Perovskite Nanocrystals, *Acc. Chem. Res.*, 2021, **54**, 707–718.

54 D. P. Nenon, K. Pressler, J. Kang, B. A. Koscher, J. H. Olshansky, W. T. Osowiecki, M. A. Koc, L.-W. Wang and A. P. Alivisatos, Design Principles for Trap-Free CsPbX3 Nanocrystals: Enumerating and Eliminating Surface Halide Vacancies with Softer Lewis Bases, *J. Am. Chem. Soc.*, 2018, **140**, 17760–17772.

55 V. K. Ravi, P. K. Santra, N. Joshi, J. Chugh, S. K. Singh, H. Rensmo, P. Ghosh and A. Nag, Origin of the Substitution Mechanism for the Binding of Organic Ligands on the Surface of CsPbBr3 Perovskite Nanocubes, *J. Phys. Chem. Lett.*, 2017, **8**, 4988–4994.

56 M. Zhang, Z. Zheng, Q. Fu, Z. Chen, J. He, S. Zhang, L. Yan, Y. Hu and W. Luo, Growth and characterization of all-inorganic lead halide perovskite semiconductor CsPbBr3 single crystals, *CrystEngComm*, 2017, **19**, 6797–6803.

57 Q. Zhang, B. Wang, W. Zheng, L. Kong, Q. Wan, C. Zhang, Z. Li, X. Cao, M. Liu and L. Li, Ceramic-like stable CsPbBr3 nanocrystals encapsulated in silica derived from molecular sieve templates, *Nat. Commun.*, 2020, **11**, 31.

58 S. Mourdikoudis, M. Menelaou, N. Fiuza-Maneiro, G. Zheng, S. Wei, J. Pérez-Juste, L. Polavarapu and Z. Sofer,

Oleic acid/oleylamine ligand pair: a versatile combination in the synthesis of colloidal nanoparticles, *Nanoscale Horiz.*, 2022, **7**, 941–1015.

59 N. V. Jadhav, A. I. Prasad, A. Kumar, R. Mishra, S. Dhara, K. R. Babu, C. L. Prajapat, N. L. Misra, R. S. Ningthoujam, B. N. Pandey and R. K. Vatsa, Synthesis of oleic acid functionalized Fe3O4 magnetic nanoparticles and studying their interaction with tumor cells for potential hyperthermia applications, *Colloids Surf., B*, 2013, **108**, 158–168.

60 F. Lan, J. Bai and H. Wang, The preparation of oleylamine modified micro-size sphere silver particles and its application in crystalline silicon solar cells, *RSC Adv.*, 2018, **8**, 16866–16872.

61 A. A. M. Brown, T. J. N. Hooper, S. A. Veldhuis, X. Y. Chin, A. Bruno, P. Vashishtha, J. N. Tey, L. Jiang, B. Damodaran, S. H. Pu, S. G. Mhaisalkar and N. Mathews, Self-assembly of a robust hydrogen-bonded octylphosphonate network on cesium lead bromide perovskite nanocrystals for light-emitting diodes, *Nanoscale*, 2019, **11**, 12370–12380.

62 R. Grisorio, M. E. Di Clemente, E. Fanizza, I. Allegretta, D. Altamura, M. Striccoli, R. Terzano, C. Giannini, M. Irimia-Vladu and G. P. Suranna, Exploring the surface chemistry of cesium lead halide perovskite nanocrystals, *Nanoscale*, 2019, **11**, 986–999.

63 J. De Roo, N. Yazdani, E. Drijvers, A. Lauria, J. Maes, J. S. Owen, I. Van Driessche, M. Niederberger, V. Wood, J. C. Martins, I. Infante and Z. Hens, Probing Solvent–Ligand Interactions in Colloidal Nanocrystals by the NMR Line Broadening, *Chem. Mater.*, 2018, **30**, 5485–5492.

64 J. Pan, S. P. Sarmah, B. Murali, I. Dursun, W. Peng, M. R. Parida, J. Liu, L. Sinatra, N. Alyami, C. Zhao, E. Alarousu, T. K. Ng, B. S. Ooi, O. M. Bakr and O. F. Mohammed, Air-Stable Surface-Passivated Perovskite Quantum Dots for Ultra-Robust, Single- and Two-Photon-Induced Amplified Spontaneous Emission, *J. Phys. Chem. Lett.*, 2015, **6**, 5027–5033.

65 J. De Roo, M. Ibáñez, P. Geiregat, G. Nedelcu, W. Walravens, J. Maes, J. C. Martins, I. Van Driessche, M. V. Kovalenko and Z. Hens, Highly Dynamic Ligand Binding and Light Absorption Coefficient of Cesium Lead Bromide Perovskite Nanocrystals, *ACS Nano*, 2016, **10**, 2071–2081.

66 G. Jones, W. R. Jackson, C. Y. Choi and W. R. Bergmark, Solvent effects on emission yield and lifetime for coumarin laser dyes, *J. Phys. Chem.*, 1985, **89**, 294–300.